Journal of Pharmaceutical Analysis 14 (2024) 100928

Contents lists available at ScienceDirect

Journal of Pharmaceutical Analysis

journal homepage: www.elsevier.com/locate/jpa

Original article

Design of a nanozyme-based magnetic nanoplatform to enhance photodynamic therapy and immunotherapy

Chen Bai [a, 1], Jiajing Liu [a, 1], Luyao Bai [a, 1], Dapeng Yao [b], Xiaofeng Li [b], Haoran Zhang [a], Dong Guo [a, *]

[a] Jiangsu Key Laboratory of New Drug Research and Clinical Pharmacy, Xuzhou Medical University, Xuzhou, Jiangsu, 221004, China
[b] Department of Radiology, Xuzhou Cancer Hospital, Xuzhou, Jiangsu, 221004, China

ARTICLE INFO

Article history:
Received 8 September 2023
Received in revised form
4 December 2023
Accepted 21 December 2023
Available online 28 December 2023

Keywords:
Nanozyme
Photodynamic therapy
Tumor microenvironment
Immunotherapy
Dual-mode tomography

ABSTRACT

The tumor microenvironment, particularly the hypoxic property and glutathione (GSH) overexpression, substantially inhibits the efficacy of cancer therapy. In this article, we present the design of a magnetic nanoplatform (MNPT) comprised of a photosensitizer (Ce6) and an iron oxide (Fe_3O_4)/manganese oxide (MnO_2) composite nanozyme. Reactive oxygen species (ROS), such as singlet oxygen ($^1O_2$) radicals produced by light irradiation and hydroxyl radicals (·OH) produced by catalysis, are therapeutic species. These therapeutic substances stimulate cell apoptosis by increasing oxidative stress. This apoptosis then triggers the immunological response, which combines photodynamic therapy and T-cell-mediated immunotherapy to treat cancer. Furthermore, MNPT can be utilized as a contrast agent in magnetic resonance and fluorescence dual-modality imaging to give real-time tracking and feedback on treatment.

1. Introduction

Nanocatalytic therapy, such as chemodynamic therapy (CDT) and photodynamic therapy (PDT), has sparked public attention in recent years [1–5]. The therapeutic effect is achieved by producing reactive oxygen species (ROS) through enzyme-like characteristics (nanozymes) in the tumor microenvironment [6,7]. Overproduction of ROS causes tumor cell apoptosis while enhancing immunogenicity [8]. However, in most solid tumors, overexpressed glutathione (GSH) promotes tumor growth by scavenging ROS [9,10]. Furthermore, the hypoxic tumor microenvironment results in a lack of oxygen (O_2), which inhibits ROS production [11,12]. Therefore, immediate attention to the mentioned problems is required to enhance the effectiveness of nanocatalytic therapy.

Numerous studies have been undertaken to improve the efficacy of nanocatalytic therapy [13–16]. A nanotechnical technique to generate ROS in tumors is an effective strategy [17–19]. The fundamental issue of this approach is maintaining high amounts of free iron while decreasing the quantity of ROS scavengers (such as GSH) [20]. Previous studies revealed that metal iron-related nanozymes (such as Fe, Mn, or Cu) can exhibit Fenton-like activity to down-regulate GSH [21–23]. Combining ferrosoferric oxide (Fe_3O_4) with manganese oxide (MnO_2) can therefore be a potential strategy for increasing the therapeutic effect. PDT, which generates ROS through photoexcitation, is a common technique in nanocatalytic treatment [24]. The effects of PDT are limited by hypoxia [25]. As a result, sufficient O_2 levels in the tumor are necessary. Manganese oxide nanozyme is typically used in PDT because of its catalase (CAT) activity, which converts hydrogen peroxide (H_2O_2) into O_2 in tumors [26,27]. Furthermore, by acting as a carrier, nanozyme can extend the retention duration of photosensitizers [28]. The generated ROS can also increase cell apoptosis and trigger immunity through extrachromosomal circular DNA elements [29].

Here, we constructed a magnetic nanoplatform (MNPT) using chlorin e6 (Ce6), bovine serum albumin (BSA)-modified MnO_2 (BSA@MnO_2), and dopamine (DPA)-modified Fe_3O_4 (DPA@Fe_3O_4) (Fig. 1). The Fe_3O_4/MnO_2 composite nanozyme generated both O_2 and hydroxyl radicals (·OH) through CAT-like and peroxidase (POD)-like activities. Ce6 acted as a photosensitizer, converting O_2 to singlet oxygen ($^1O_2$) and providing photodynamic effects. Furthermore, the GSH-depletion property obtained by MNPT through Fenton/Fenton-like mechanisms. The MNPT in the tumor microenvironment increased cell apoptosis through the production of ROS and the depletion of GSH. This induced cell apoptosis

* Corresponding author.
E-mail address: guo@xzhmu.edu.cn (D. Guo).
[1] These authors contributed equally to this work.

https://doi.org/10.1016/j.jpha.2023.12.018

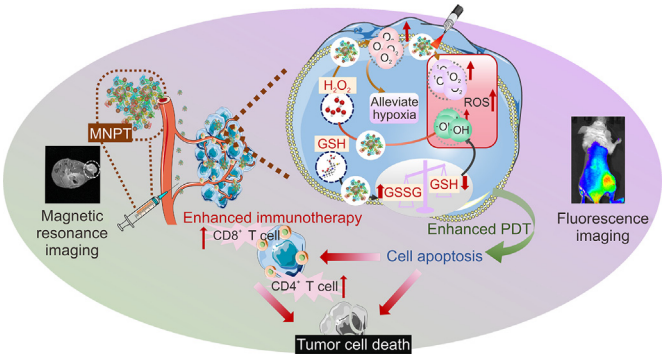

Fig. 1. The schematic diagram of tumor therapy enhancement by magnetic nanoplatform (MNPT). ROS: reactive oxygen species; GSH: glutathione; GSSG: oxidized glutathione; PDT: photodynamic therapy.

activated a T-cell-mediated immunological response, combining PDT and T-cell-mediated immunotherapy. MNPT could give real-time monitoring and treatment feedback for dual-modality fluorescence-magnetic resonance imaging.

2. Materials and methods

2.1. Materials

The reagents used are purchased from regular domestic market agents and have not undergone any pre-treatment. Anhydrous ethanol, chloroform, potassium permanganate, dimethyl sulfoxide, hydrochloric acid, disodium hydrogen phosphate dodecahydrate, sodium acetate trihydrate, sodium dihydrogen phosphate dihydrate, acetic acid, anhydrous sodium sulfite, H_2O_2 and 3,3′,5,5′-tetramethylbenzidine (TMB) were obtained from Sinopharm Chemical Reagent Co., Ltd. (Beijing, China). Iron acetylacetonate (98%) was acquired from Sigma Aldrich Trading Co., Ltd. (Shanghai, China). Dibenzyl ether (97%) was obtained from Alfa Aesar Chemicals Ltd. (Heysham, UK). Oleic acid amide (OAm) (≥90%) and dopamine hydrochloride were obtained from Adamas Reagents Ltd. (Shanghai, China). BSA was obtained from Shanghai yuanye Bio-Technology Co., Ltd. (Shanghai, China). Ce6 (94%) and GSH (98%) were obtained from Shanghai Maclean Biochemical Technology Co., Ltd. (Shanghai, China). The 4T1 cells and RAW 264.7 cells used during the experiments were acquired from the Cell Bank of the Chinese Academy of Sciences (Shanghai, China). The Single-Organic State Oxygen Green Fluorescent Probe (SOSG) Kit, Lyso-Tracker Green, Hoechst 33342, 2′,7′-dichlorofluorescin diacetate (DCFH-DA) probes, 4′,6-diamidino-2-phenylindole dihydrochloride (DAPI) solution, and, Annexin V-FITC Apoptosis Detection Kit were obtained from Beyotime Biotechnology (Shanghai, China). The Reduced Glutathione Content Assay Kit, the CCK-8 solution and, 4% paraformaldehyde were obtained from Solarbio Life Sciences (Beijing, China). Phosphate buffered saline (PBS) and DMEM/F12 culture medium were obtained from KeyGen BioTECH (Nanjing, China). Fetal bovine serum (FBS) was obtained from Gibco Inc. (Carlsbad, CA, USA). PE/Cy7 anti-CD45, APC anti-CD3, FITC anti-CD4 and, PE anti-CD8 antibodies were obtained from Becton, Dickinson and Company (Franklin Lakes, NJ, USA).

2.2. Instrumentation

Characterizations of the morphology and size of magnetic nanoparticles were measured by transmission electron microscopy (TEM; JEM2100, JEOL, Tokyo, Japan). Characterizations of the hydrodynamic size of magnetic nanoparticles were measured by a dynamic light scattering (DLS; ZS 90, Malvern Zetasizer, London, UK). The UV spectrums were recorded using a UV-visible spectrophotometer (UV-3600, Shimadzu, Kyoto, Japan). The fluorescence spectrums were recorded through the Fluorospectro photometer (F-4600, Hitachi, Tokyo, Japan). The concentrations of different nanoparticles were carried out on inductively coupled plasma optical emission spectrometer (ICP-MS; NexION 300X, PerkinElmer, Boston, MA, USA). The X-ray diffractometer (XRD; Ultima IV, Rigaku Ultima, Tokyo, Japan) was used to measure the XRD of DPA@Fe_3O_4, BSA@MnO_2, and MNPT. A 660 nm laser (0.9 A, 500 mW/cm^2) was obtained from Viasho Technology Co., Ltd. (Beijing, China) and used for laser irradiation. The lysosomal co-localization assay was measured by confocal microscope (STELLARIS 5, Leica, Wetzlar, Germany). The relaxivities were measured using a 3.0 T MR scanner (Verio, Siemens, Munich, Germany). The generation of O_2 was measured by a dissolved oxygen electrode (JPSJ-605F) which was obtained from Shanghai Yi Electrical Scientific Instruments Co., Ltd (Shanghai, China). A fluorescent microscope (IX-73, Olympus Corporation, Tokyo, Japan) was used to examine the fluorescence intensity in cells. The fluorescence intensity of cells was examined by flow cytometry (CantonII, BD, Franklin Lakes, NJ, USA).

2.3. Synthesis of MNPT

An oil-soluble Fe_3O_4 nanoparticle was synthesized using a high-temperature thermal decomposition method. 60 mL of OAm, 40 mL of dibenzyl ether, and 5.25 g of iron acetylacetonate were mixed thoroughly. Under nitrogen protection and condenser reflux, the reaction was set up to warm up. Upon removing the heating element at the end of the experiment, the reaction restored room temperature quickly. It was successful in producing oil-soluble Fe_3O_4 nanoparticles after washing with magnetic separations.

Water-soluble DPA@Fe_3O_4 was produced through the ligand exchange method. In a 250 mL three-necked round-bottom flask, 40 mg of dopamine hydrochloride, 4 mL of anhydrous dimethylsulfoxide, and 4 mL of chloroform solution were added. The reaction was sonicated at 70 °C and stirred mechanically at a rate of 1,000 rpm/min. Oil-soluble Fe_3O_4 nanoparticles (20 mg) were applied dropwise. A 2 h reaction was followed by the addition of 2 mL of chloroform and a centrifugation at 5,000 rpm. Nitrogen gas was used to dry the precipitate. DPA@Fe_3O_4 is produced by dissolving it in water at pH 4.0.

BSA@MnO_2 is created by slowly adding a solution of bovine serum protein to a solution of potassium permanganate at 37 °C with magnetic stirring for 2 h. After adding 2 mg BSA@MnO_2, 1.5 mL ultrapure water, and 5 mg Ce6, the mixture was shaken for 4 h at 37 °C. To obtain the MNPT, 4 mg DPA@Fe_3O_4 was then added. Before concentration, the Ce6 and BSA@MnO_2 without coupling on MNPT were separated via ultrafiltration (100 kDa). The concentration of Fe and Mn was measured by ICP-MS. The iron concentration of DPA@Fe_3O_4 was 4.64 mg/mL. The manganese concentration of BSA@MnO_2 was 2.78 mg/mL. The concentration of Ce6 was 0.23 mg/mL. The iron concentration of MNPT without Ce6 modification (BSA@Fe_3O_4/MnO_2) was 0.22 mg/mL. The iron concentration of MNPT was 0.22 mg/mL.

2.4. Relaxivity test of magnetic resonance imaging (MRI)

MNPT and BSA@MnO_2 were diluted with 10 mM GSH solution to various concentrations (1 mol/mL, 0.5 mol/mL, 0.25 mol/mL, 0.125 mol/mL, and 0.0625 mol/mL). The r_1 value relaxivities were measured using a 3.0 T MR scanner.

2.5. In vitro release of Ce6

A standard curve was created using various Ce6 concentrations. The release of Ce6 from MNPT was investigated using the standard curve.

2.6. $^1O_2$ generation capacity of MNPT

The SOSG Kit was used to obtain the results. The SOSG solution (100 μM) contained 100 μM H_2O_2 with various concretions of MNPT and Ce6. Following laser irradiation, the $^1O_2$ generation capacity was measured at 504 nm.

2.7. GSH depletion capacity of MNPT

The Reduced Glutathione Content Assay Kit was used to conduct the test. Following an incubation period with GSH (10 mM) in various buffer solutions, the absorbance of the solution was determined.

2.8. Enzyme-like activity of MNPT

The POD-like enzymatic activity assays of MNPT were measured at room temperature using H_2O_2 (100 μM), GSH (10 mM), and TMB (0.5 mM) in 0.02 M buffer solutions.

Using a dissolved oxygen electrode, the produced O_2 was measured to evaluate the CAT-like enzymatic activity of MNPT. In 0.02 M buffer solutions, H_2O_2 (100 μM) was added in addition to various nanoparticles for measurement.

2.9. Hemolytic test of MNPT

Human blood was taken from the Institute of Cancer Biotherapy. Various quantities of MNPT were incubated with a 10% red blood cell suspension for 24 h. The absorption value was obtained at 540 nm. The saline group was utilized as a negative control. The distilled water group was utilized as a positive control.

2.10. Cytotoxicity test

RAW 264.7 cells were cultured in DMEM/F12 medium supplemented with 10% FBS at 37 °C and 5% carbon dioxide (CO_2). Into each well of a 96-well plate, 5×10^3 cells in the logarithmic growth phase were added. After 24 h of cell growth, various iron amounts of MNPT were applied. The CCK-8 solution added media was replaced after a 24 h incubation period. Measurements were made of the absorption values at 450 nm.

4T1 cells were grown at 37 °C with 5% CO_2 in DMEM/F12 media containing 10% FBS. Into each well of a 96-well plate, 5×10^3 cells in the logarithmic growth phase were added into each well of a 96-well plate. After a 6 h incubation period, the laser group was exposed to radiation for 15 s each well. The CCK-8 solution added media was replaced after a 24 h incubation period. The absorption values were measured at 450 nm.

2.11. Phagocytosis assay for MNPT

A 6-well plate was seeded with 2×10^5 logarithmic growth phase 4T1 cells. After a 24 h cell growth period, the 4T1 cells were cultured with the same volume of Ce6 and MNPT. For staining, a DAPI solution was applied. Using a fluorescent microscope, the cells were examined at 0, 2, 4, and 6 h.

2.12. Lysosomal co-localization assay

In the logarithmic growth phase, 1×10^4 4T1 cells were inoculated onto the confocal dish. PBS and MNPT groups were created for the tests. Before observation, Lyso-Tracker Green and Hoechst 33342 were applied to the confocal dishes.

2.13. Cell scratch test for MNPT

A 6-well plate was seeded with 2×10^5 logarithmic growth phase 4T1 cells. After 24 h, two evenly spaced scratches were produced in the 6-well plate. Different treatment groups were established for the tests. After a 6 h incubation period, the laser group was exposed to radiation for 15 s each well. A fluorescent microscope was used to record the images.

2.14. Reactive oxygen content detection in vitro

A 6-well plate was seeded with 2×10^5 logarithmic growth phase 4T1 cells. The experiments were divided into different treatment groups. After a 6 h incubation period, the laser group was exposed to radiation for 15 s each well. After 24 h incubation, DCFH-DA probes were added and the fluorescence intensity of cells was examined using a fluorescent microscope and flow cytometry.

2.15. GSH content detection in vitro

A 6-well plate was seeded with 2×10^5 logarithmic growth phase 4T1 cells. The experiments were divided into different treatment groups. After a 6 h incubation period, the laser group was exposed to radiation for 15 s each well. The cells were collected after 24 h incubation. The absorption values of the supernatant were measured by using the Reduced Glutathione Content Assay Kit.

2.16. Apoptosis assay for MNPT

A 6-well plate was seeded with 2×10^5 logarithmic growth phase 4T1 cells. The experiments were divided into different treatment groups. After a 6 h incubation period, the laser group was exposed to radiation for 15 s each well. After 24 h incubation, the cells were collected and stained by annexin V and propidium. The apoptosis was determined by flow cytometry.

2.17. Animal model

The Balb/c mice (6–7 weeks, female) used in the experiments were provided by the Experimental Animal Centre of Xuzhou Medical University Main Campus. All animal experiments involved in the study were approved by the Ethics Committee of Xuzhou Medical University and all experimental operations were carried out in strict accordance with the Experimental Animal Regulations of Xuzhou Medical University (IACUC Number: 202209S27). The mouse breast cancer model was created by subcutaneously injecting 4T1 cells (5×10^6) into the back of the mice, and 5 days later, the tumor size of the mice had grown to 60 mm^3.

2.18. In vivo treatment protocol in animals

The 40 mice were randomly divided into eight treatment groups. 0.48 mg [Fe]/kg (0.5 mg [Ce6]/kg) mice weight materials were injected surrounding the tumor on the days of 1, 3, 5, and 7. The mice of groups treated with laser irradiation were irradiated for 5 min at 6 h and 24 h after injecting materials.

2.19. Histochemical and immunohistochemistry analysis

After the treatment, mice from each treatment group were executed. Both the tumor tissues and major organs were removed. All isolated tissues were fixed in 4% paraformaldehyde before being sectioned with paraffin. Hematoxylin–Eosin (HE)

staining was applied to the sections to determine the tissue's pathological condition. To assess the histopathological and immunological results, sections were also stained using $CD4^+$, $CD8^+$, terminal deoxynucleotidyl transferase mediated dUTP nick-end labeling (Tunel), proapoptotic protein (Bax), and B-cell lymphoma 2 (Bcl-2).

2.20. The antitumor immunity in vivo

After the whole treatment, the tumor tissues were homogenized in PBS to get the single-cell suspensions. The single-cell suspensions were stained with PE/Cy7 anti-CD45, APC anti-CD3, FITC anti-CD4, and PE anti-CD8, respectively. The analysis was used by the flow cytometry.

2.21. In vivo MRI experiments

MRI of tumor-bearing mice was performed by using 3.0 T MRI equipment and small animal-specific coils. Tumor-bearing mice were injected surrounding the tumor with 0.48 mg [Fe]/kg mice weight and anesthetized to record the T_1-weighted MRI images at 0 h and 4 h. T_1-weighted MRI sequences: repetition time of 600 ms, echo time of 10 ms, flip angle of 20°, and layer thickness of 4 mm.

The contrast-to-noise ratio (CNR) uses the signal ratio between the tumor site and the surrounding normal tissue to detect signal changes. The signal-to-noise ratio (SNR) between various tissues can be obtained by reading the ratio of the signal value (SI) in a selected area to the background signal value (SD) in that area. Based on equation (1) and (2), we can calculate the degree of signal change CNR at the tumor site compared to normal tissue.

$$SNR = SI/SD \quad (1)$$

$$CNR = |SNR_{tumor} - SNR_{normal}|/SNR_{tumor} \quad (2)$$

2.22. Statistical analysis

To determine the significance of the experimental data, a one-sample *t*-test statistical analysis was used. The level of significance was set at *P*-value of 0.05. The information was denoted as $^{*}P < 0.05$, $^{**}P < 0.01$, and $^{***}P < 0.001$.

3. Results and discussion

3.1. Synthetic characterization of MNPT

Oil-soluble magnetic Fe_3O_4 was synthesized by a high-temperature thermal decomposition method. The hydrophobic ligands were exchanged with DPA to synthesize the water-soluble nanomaterial DPA@Fe_3O_4. However, this material was stable only under acidic conditions (pH $\leq$ 4) [30]. BSA@MnO_2 was added to create BSA@Fe_3O_4/MnO_2, which improved the stability of DPA@Fe_3O_4 and served as a bridge to couple with other compounds. Furthermore, Ce6 was attached to the surface of the nanoparticles to construct the MNPT (Fig. 2A). According to TEM images (Fig. S1A), DPA@Fe_3O_4 was around 5 nm in size, and there was no visible aggregation among the well-dispersed particles. TEM was used to examine the morphology of BSA@MnO_2 as shown in Fig. S1B. The MNPT size did not alter considerably after further modification (Fig. 2B). The distinctive absorption peaks of MNPT in XRD were consistent with those of DPA@Fe_3O_4 and BSA@MnO_2, suggesting that surface modification exhibited minimal impact on the nanoparticles' original structure (Fig. 2C). Compared to other nanoparticles, the MNPT (Fig. S2) had a slightly greater hydrodynamic size. Because of its appropriate size, MNPT retention length could be extended *in vivo* [31]. Furthermore, MNPT could remain stable in cell culture media and water for 7 days (Fig. S3).

The fluorescence characteristics of MNPT were evaluated for usage as a contrast agent in fluorescent imaging. In the UV spectrum (Fig. S4) and fluorescence spectrum (Figs. 2D and E), the synthesized MNPT displayed absorption peaks similar to those of Ce6. These findings showed that Ce6 was successfully modified in the MNPT and its fluorescence characteristics were unaffected during the production process. Furthermore, the contrast enhancement provided by the MNPT for MRI was assessed. The relaxivities (r_1 values) of MNPT and BSA@MnO_2 were 9.12 and 9.17 $mM^{-1} \cdot s^{-1}$, respectively (Figs. 2F and G). It indicated that MNPT could be used as a T_1-weighted contrast agent in MRI. Therefore, the synthesized MNPT exhibited enhanced contrast for fluorescence-magnetic resonance dual-modality imaging.

3.2. Functional characterization of MNPT

Although the tumor microenvironment is weakly acidic (pH 6.8), the pH of lysosomes in tumor cells is approximately 4.5–5.5 [32,33]. As a result, we used three different pH buffers (5, 6, and 7) to recreate the tumor microenvironment and lysosomes. As demonstrated in Fig. 3A, the release of Ce6 from MNPT was confirmed. The most Ce6 was released in the pH 5 buffer solution. The results indicated that tumor cells could contain more Ce6 than normal cells. Following laser irradiation, the generation of $^1O_2$ by MNPT and Ce6 was tested and displayed in Fig. 3B. In the same photosensitizer concertation, MNPT produced more $^1O_2$ than Ce6. Tumors also have high levels of GSH, which promotes tumor growth [34,35]. As demonstrated in Fig. 3C, the metal oxide nanoparticles dramatically lowered GSH levels. Compared to BSA@MnO_2 and DPA@Fe_3O_4, MNPT showed superior GSH removal capabilities.

According to earlier research, metal oxidase nanoparticles are nanozymes that can exhibit intrinsic enzyme activity [36,37]. POD activity initially appeared in Fe_3O_4 nanozymes, and the ·OH produced by nanozymes was found to be important in cancer treatment [38]. MNPT could generate high levels of ·OH across the varied pH situations Figs. 3D–F). POD activity from the MNPT increased as pH decreased. Therefore, more ·OH was produced by MNPT in tumor tissue compared to normal tissue. MNPT could generate ·OH and imitate CAT activity, which induces apoptosis in tumor cells and reduces hypoxia. Similar to BSA@MnO_2, MNPT produced a significant quantity of O_2 when combined with H_2O_2 Figs. 3G–I). Tumor growth is attributed to increased levels of H_2O_2 in solid tumors [39]. Thus, MNPT reduced H_2O_2 levels while increasing O_2 levels to limit tumor growth and improve the PDT effect.

3.3. Therapeutic effect of MNPT in vitro

A hemolytic test was performed with the MNPT, and the results are shown in Fig. S5 and Table S1. There was no agglutination of red blood cells after coincubation with MNPT. Hemolysis rates were below 5% with the different concentrations of MNPT tested. The low hemolysis rates indicated that MNPT was compatible with the blood [40]. In addition, the cytotoxicity of MNPT was determined in RAW 264.7 cells (Fig. S6). After 24 h of incubation with various concentrations (0–100 μg [Fe]/mL) of MNPT, cell viability was above 80%. The hemolysis rate and low cytotoxicity indicated that MNPT was biocompatible and suitable for in vitro and in vivo experiments.

4T1 cells were used to test the uptake of Ce6, and results are shown in Figs. 4A and B. After 6 h of coculturing with MNPT and

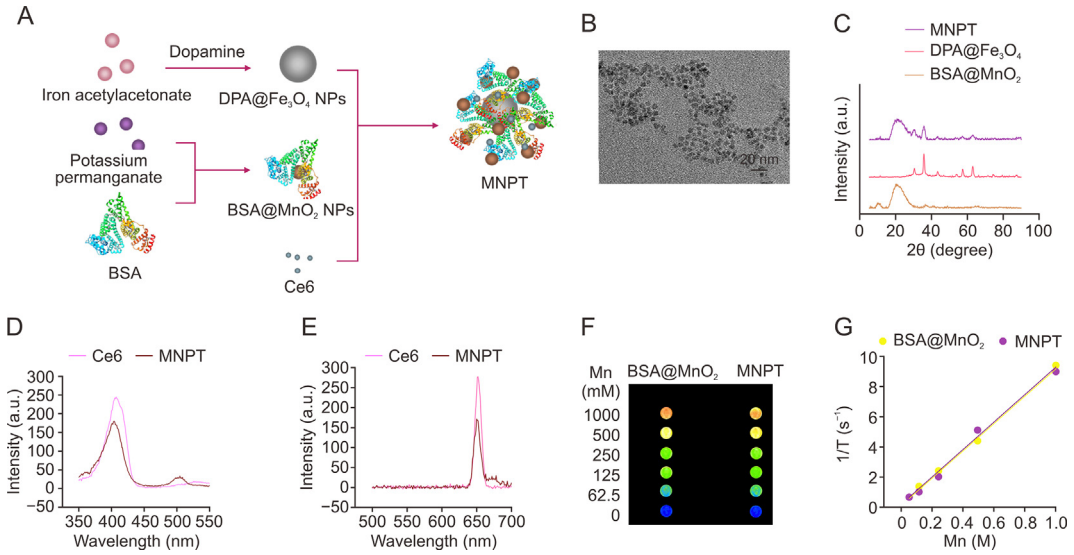

Fig. 2. (A) Schematic illustration of a magnetic nanoplatform (MNPT) preparation. (B) Transmission electron microscopy (TEM) images of MNPT. (C) X-ray diffraction (XRD) of nanomaterials including BSA@MnO_2, DPA@Fe_3O_4, and MNPT. (D) The fluorescence excitation spectrum of Ce6 and MNPT. (E) The fluorescence emission spectra of Ce6 and MNPT. (F) T_1-weighted magnetic resonance images of BSA@MnO_2 and MNPT. (G) The relaxivities of r_1 values in BSA@MnO_2 and MNPT. BSA: bovine serum albumin; DPA@Fe_3O_4: dopamine modified iron oxide; BSA@MnO_2: bovine serum albumin modified manganese oxide; Ce6: chlorin e6.

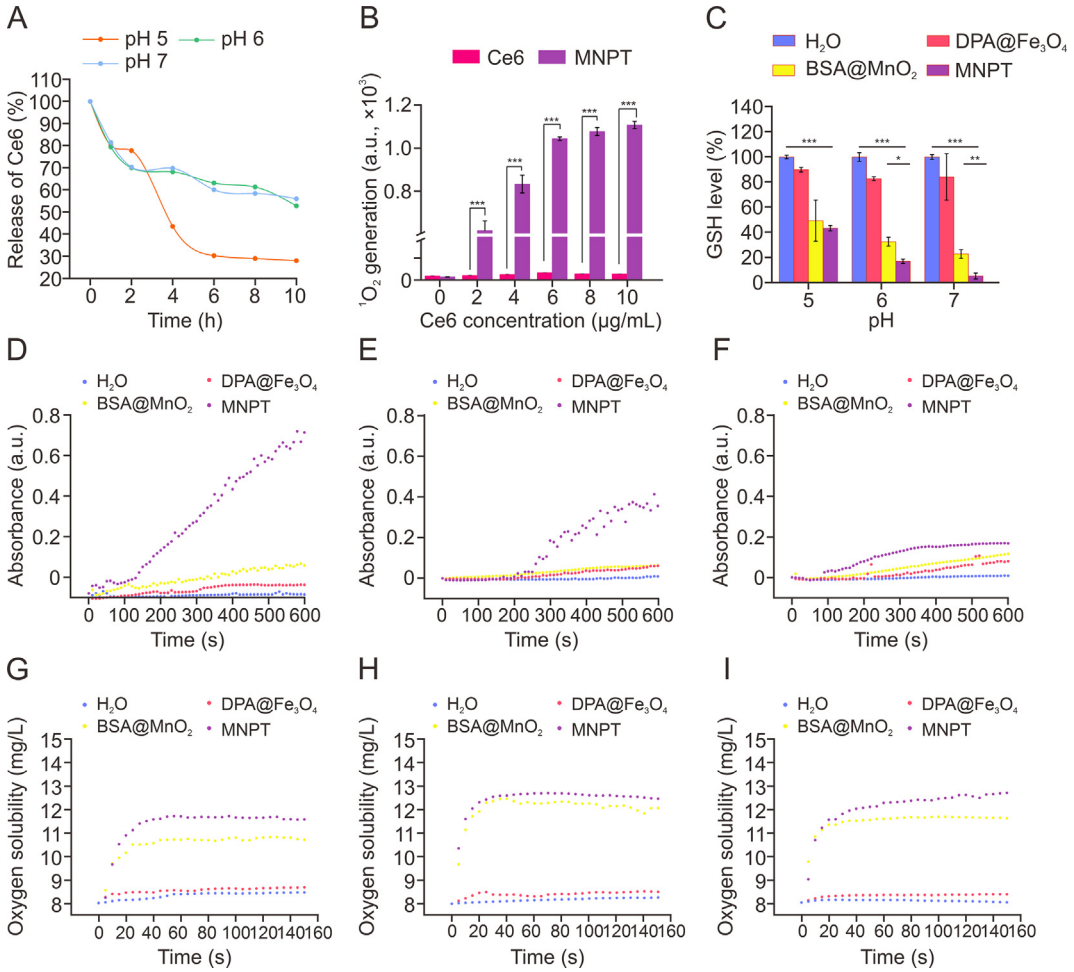

Fig. 3. (A) The released curve of chlorin e6 (Ce6) from magnetic nanoplatform (MNPT) with different pH values. (B) Concentration-dependent singlet oxygen ($^1O_2$) production by Ce6 and MNPT. (C) Illustration of glutathione (GSH) depletion by BSA@MnO_2, DPA@Fe_3O_4, MNPT, and H_2O. (D–F) The peroxidase (POD) activity of BSA@MnO_2, DPA@Fe_3O_4, MNPT and, H_2O in buffer solutions with pH values of 5.0 (D), 6.0 (E) and 7.0 (F). (G–I) The catalase (CAT) activity of BSA@MnO_2, DPA@Fe_3O_4, MNPT and, H_2O in buffer solutions with pH values of 5.0 (G), 6.0 (H) and 7.0 (I). Data shown are the mean ± standard deviation (SD) ($n = 3$). $^*P < 0.05$, $^{**}P < 0.01$, $^{***}P < 0.001$. DPA@Fe_3O_4: dopamine modified iron oxide; BSA@MnO_2: bovine serum albumin modified manganese oxide.

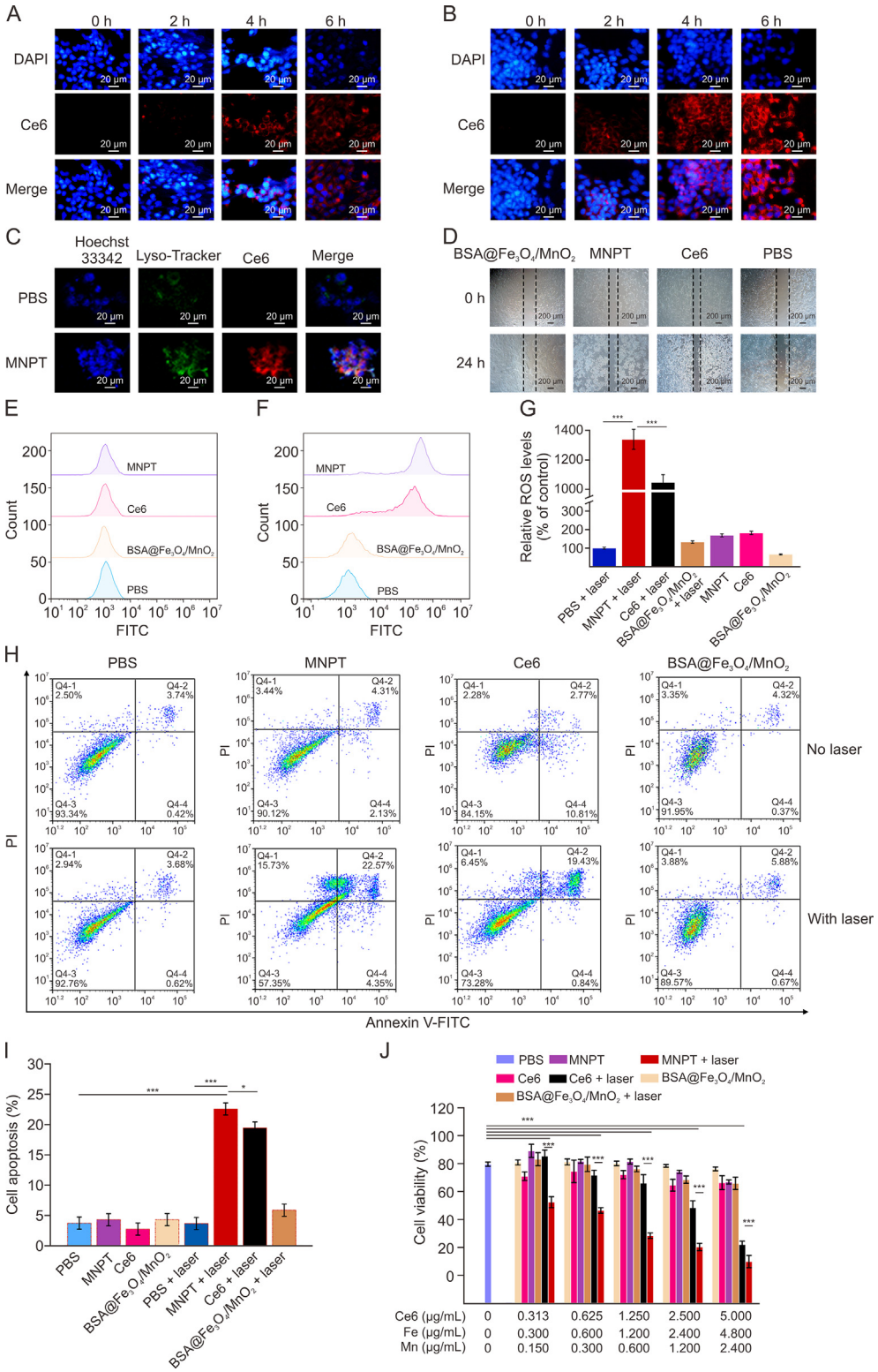

Fig. 4. (A, B) The cell phagocytosis images of chlorin e6 (Ce6) (A) and magnetic nanoplatform (MNPT) (B) in 4T1 cells. (C) Lysosomal co-localization assay of MNPT and phosphate buffered saline (PBS) with 4T1 cells. (D) The images of cell scratch experiments under laser irradiation with different treatment groups. (E, F) The generation of reactive oxygen species (ROS) without laser irradiation (E) and with laser irradiation (F). (G) Quantification of ROS level in different treatment groups. (H) Cell apoptosis of 4T1 cells with different treatment groups by flow cytometry. (I) Quantification of apoptosis in 4T1 cells of different treatment groups. (J) Cell viability of 4T1 cells with different treatment groups. Data shown are the mean ± standard deviation (SD) ($n = 3$). $^{*}P < 0.05$, $^{***}P < 0.001$. BSA@Fe_3O_4/MnO_2: MNPT without Ce6 modification; DAPI: 4′,6-diamidino-2-phenylindole dihydrochloride; FITC: fluorescein isothiocyanate isomer I; PI: propidiumiodide.

free Ce6, negligible red fluorescence was observed in the cells treated with free Ce6. However, after 4 h of incubation with MNPT, red fluorescence surrounding the cells appeared, and the fluorescence intensity became stronger after 6 h of incubation. Compared with free Ce6, the Ce6 connected to the MNPT was phagocytosed more by 4T1 cells. Better PDT results are seen when tumor cells phagocytose a larger quantity of Ce6. Confocal microscopy was used to examine the localization of MNPT in 4T1 cells (Fig. 4C). MNPT was found at the lysosome after a 6 h co-culture with 4T1 cells. A cell scratch experiment was carried out to confirm that the

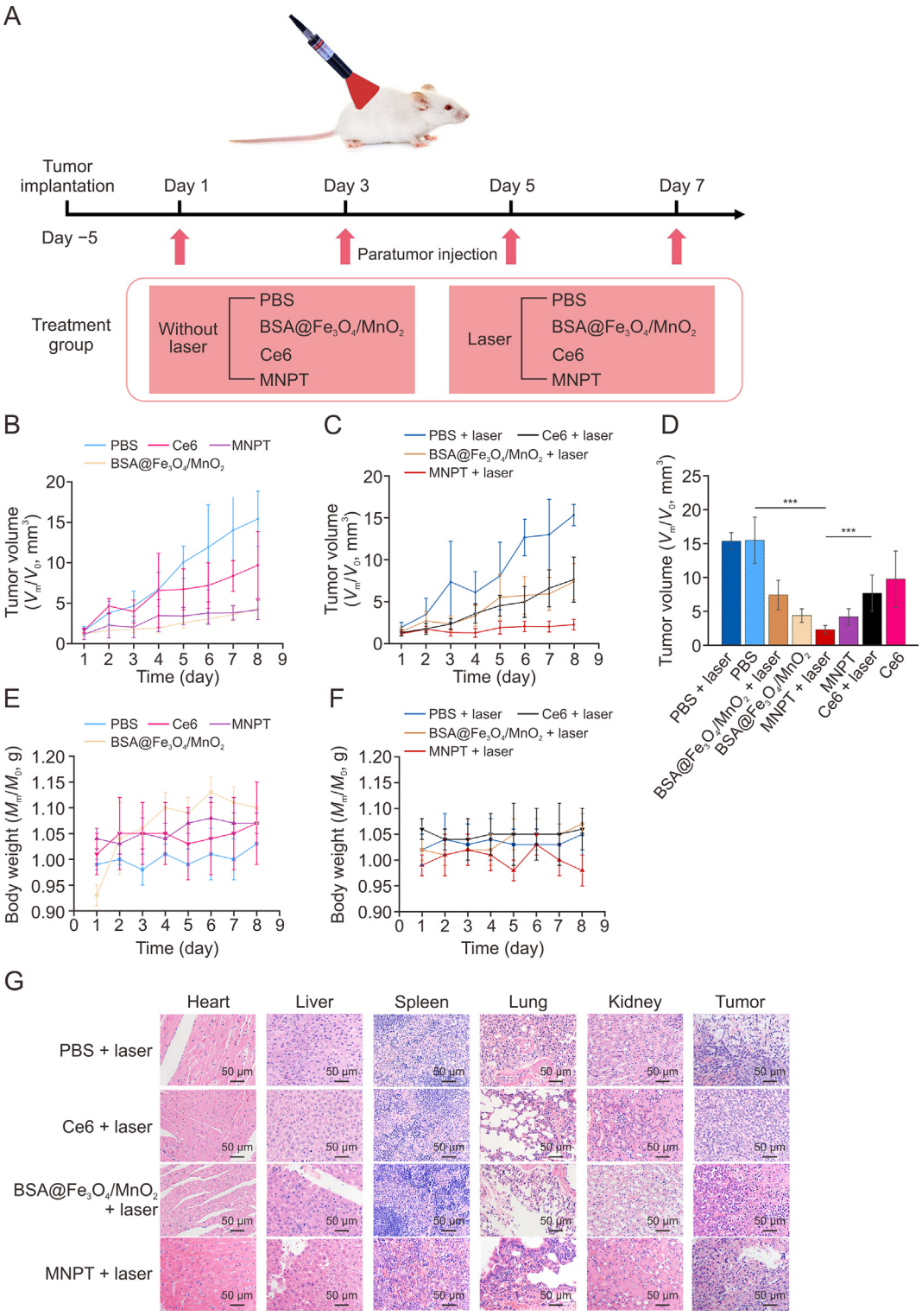

Fig. 5. (A) The treatment scheme for tumor-bearing mice. (B, C) The average tumor growth kinetics of tumor-bearing mice without laser irradiation (B) and with laser irradiation (C). (D) Tumor volume of tumor-bearing mice (the last day of the treatment cycles). (E, F) The body weight of tumor-bearing mice without laser irradiation (E) and with laser irradiation (F). (G) Hematoxylin–eosin (HE) staining images of the main organs and tumor tissues of tumor-bearing mice treated with laser irradiation. Data shown are the mean ± standard deviation (SD) ($n = 5$). $^{***}P < 0.001$. MNPT: magnetic nanoplatform; Ce6: chlorin e6; BSA@Fe_3O_4/MnO_2: MNPT without Ce6 modification; PBS: phosphate buffered saline.

nanoplatform can prevent tumor cell migration (Figs. 4D and S7). The results showed that the migration of tumor cells was reduced by MNPT combined with laser irradiation.

The ROS levels in 4T1 cells were determined using DCFH-DA probe and flow cytometry. Cells were treated with PBS, BSA@Fe_3O_4/MnO_2, free Ce6, and MNPT for 24 h. As shown in Figs. 4E and F, without laser irradiation, the level of ROS in cells was comparable among treatment groups. When the cells were treated with PBS and BSA@Fe_3O_4/MnO_2, laser irradiation did not affect the level of ROS. However, laser irradiation increased the fluorescence of DCFH-DA in cells treated with free Ce6 and MNPT (Fig. S8). The ROS in cells treated with MNPT was higher than in cells treated with free Ce6 under laser irradiation (Fig. 4G). A GSH consumption experiment *in vitro* was also conducted, as shown in Fig. S9. MNPT combined with laser irradiation could consume more GSH in tumor cells than free Ce6. The abovementioned results demonstrated that MNPT combined with laser irradiation could generate ROS and consume glutathione to enhance the tumor-killing effect.

The apoptosis of 4T1 cells was determined by flow cytometry, and the results are shown in Figs. 4H, 4I and S10. Without laser irradiation, the level of apoptosis in cells was not significantly changed after treatment with PBS, BSA@Fe_3O_4/MnO_2, free Ce6 or MNPT for 24 h. After laser irradiation, cell apoptosis was triggered by free Ce6 and MNPT. The apoptosis level of cells treated with MNPT accompanied by laser irradiation was the highest. Moreover, apoptosis was related to the concentration of MNPT. Similar results were found from cell viability experiments, as shown in Fig. 4J. MNPT strongly inhibited cell viability, and the effect improved with increasing concentration.

3.4. Therapeutic effect of MNPT in vivo

To evaluate the tumor-killing effect of the synthesized MNPT *in vivo*, we established a mouse breast cancer model by subcutaneously implanting tumors (Fig. S11). A schematic of the experimental process is shown in Fig. 5A. Forty mice were divided into eight treatment groups: PBS, BSA@Fe_3O_4/MnO_2, MNPT, free Ce6, PBS with laser, BSA@Fe_3O_4/MnO_2 with laser, MNPT with laser, and free Ce6 with laser. These therapeutic materials are injected surrounding the tumor. The tumor size and animal body weight were recorded for eight days. As expected, except for the PBS and PBS with laser irradiation groups, the tumor sizes in the other groups were inhibited. The MNPT with the laser group showed dramatic inhibition (Figs. 5B–D). The mouse survival time of the MNPT with laser group was notably prolonged compared with that of the PBS with laser and Ce6 with laser groups (Fig. S12). The better tumor-killing effect of MNPT with laser irradiation was attributed to the fact that MNPT could alleviate hypoxia and prolong the retention time of Ce6 in the tumor site. The mouse body weights did not change significantly during treatment (Figs. 5E and F). After eight days of treatment, the organs and tumors were removed, as shown in Figs. S13 and S14. The HE staining experiments were performed on the removed organs and tumor tissues (Figs. 5G and S15). These results demonstrated that the main organs, including hearts, livers,

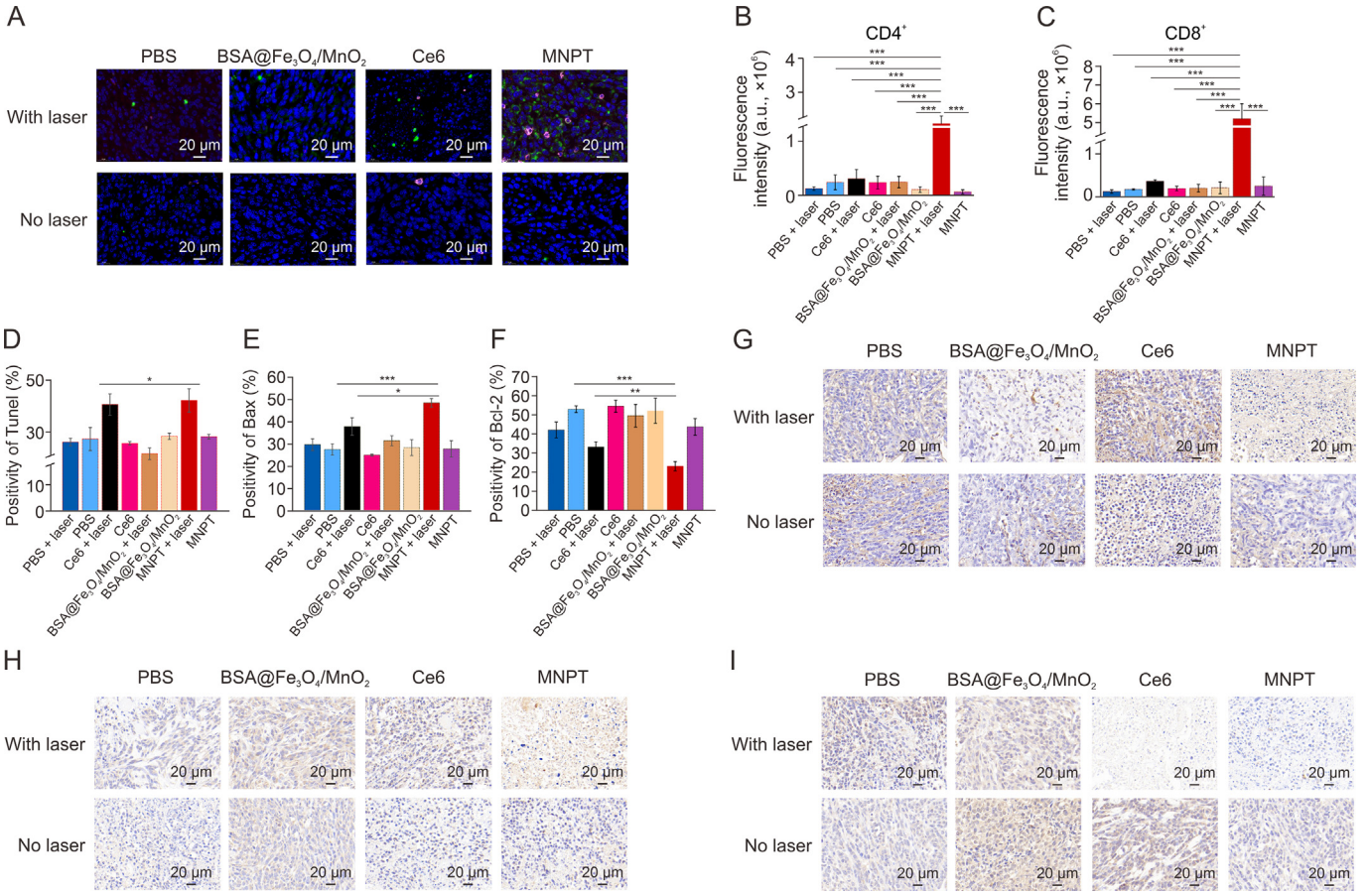

Fig. 6. (A) Immunofluorescence staining images of tumor tissue. (B, C) The quantitative analysis of $CD4^+$ (B) and $CD8^+$ (C). (D–F) Quantitative analysis of terminal deoxynucleotidyl transferase mediated dUTP nick-end labeling (Tunel) (D), proapoptotic protein (Bax) (E), and B-cell lymphoma 2 (Bcl-2) (F) in tumor tissue. (G–I)) Tunel staining (G), Bax staining (H), and Bcl-2 staining (I) of tumor tissue. Data shown are the mean ± standard deviation (SD) ($n = 5$). $^*P < 0.05$, $^{**}P < 0.01$, $^{***}P < 0.001$. MNPT: magnetic nanoplatform; Ce6: chlorin e6; BSA@Fe_3O_4/MnO_2: MNPT without Ce6 modification; PBS: phosphate buffered saline.

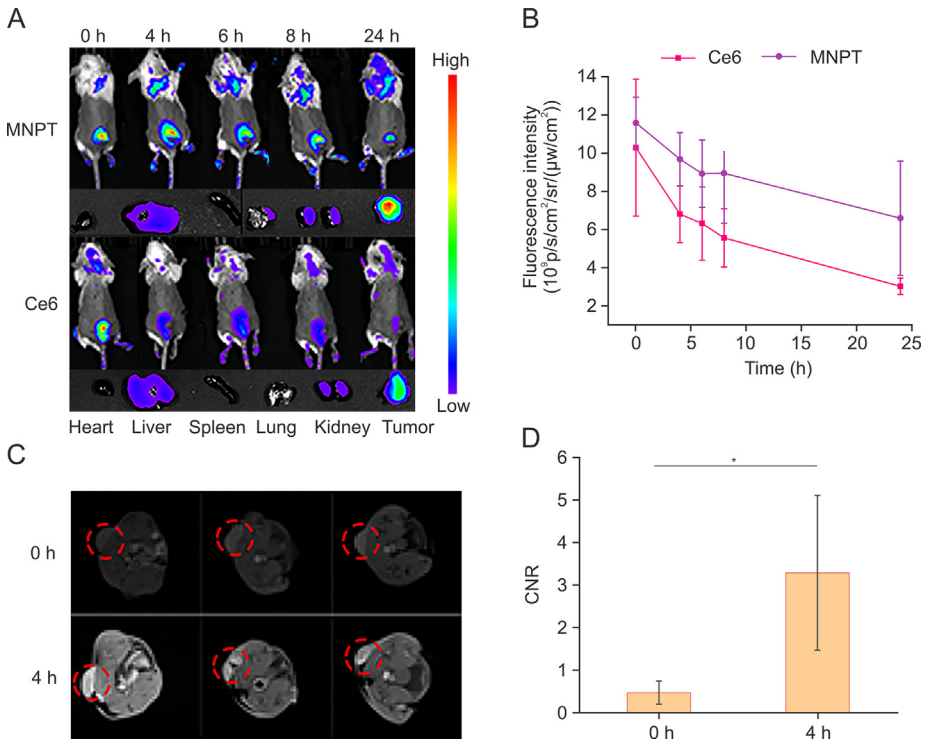

Fig. 7. (A) Fluorescence imaging of tumor-bearing mice treated with magnetic nanoplatform (MNPT) and chlorin e6 (Ce6). (B) Quantification of fluorescence intensity of tumors treated with MNPT and Ce6. (C) T1-weighted magnetic resonance images (MRI) of tumor-bearing mice treated with MNPT. (D) The contrast-to-noise ratio (CNR) in the tumor site treated with MNPT. Data shown are the mean ± standard deviation (SD) ($n = 3$). $^{*}P < 0.05$.

spleens, lungs, and kidneys, were not remarkably changed during treatment, indicating that the therapeutic materials did not exhibit significant toxicity.

Because $CD4^+$ helper and $CD8^+$ cytotoxic T lymphocytes play critical roles in immunology by killing tumor cells [41], we labeled tumor tissues from different therapy groups with CD4 and CD8 antibodies for immunohistochemical labeling. The areas stained green and pink, respectively, indicated the expression of CD4 and CD8 (Figs. 6A–C). Except for the group injected with MNPT and laser irradiation, there was no visible staining in the tumors. Tumors treated with MNPT under laser irradiation showed high expression of CD4 and CD8. Similar results were obtained in the $CD8^+$ T cell and $CD4^+$ T cell cytometry (Fig. S16).

Wang and co-workers [29] reported that extrachromosomal circular DNA fragments can induce cell death in T-cell-mediated immunological responses. We hypothesized that the improved immunotherapy was due to tumor apoptosis. Consequently, Bcl-2, Bax, and Tunel immunohistochemical staining at the tumor site have also been identified and displayed in Figs. 6D–I. The MNPT laser therapy group had decreased Bcl-2 expression. The expression of Bax and Tunel was higher in tumors treated with MNPT under laser irradiation compared to another treatment group. These results suggested that using MNPT for PDT could promote tumor cell apoptosis and facilitate the T-cell-mediated immune-killing effect. In addition, an acute toxicity test assessed the toxicity of MNPT. Fig. S17 shows the results of routine blood examinations for white blood cell, red blood cell, hemoglobin, mean corpuscular volume, mean corpuscular hemoglobin, and mean corpuscular hemoglobin concentration. There was no visible toxicity after 7 days of consecutive dosing of MNPT.

3.5. *In vivo optical imaging and MRI*

The application of Ce6 is limited because of its poor bioavailability and residence time [42]. The residency period of MNPT and Ce6 in tumor-bearing mice was evaluated by fluorescence imaging, as shown in Figs. 7A and B. MNPT and Ce6 were administered into two experimental groups. The fluorescence intensity in the MNPT group remained high at 8 h post-injection, but it gradually dropped in the Ce6 group. 24 h after injection, there was no fluorescence in the Ce6 group. However, fluorescence was still noticed in the MNPT group. To improve the PDT effect, the photosensitizer treated with MNPT may have a longer retention time in the tumor. In addition, MNPT served as a T1-weighted MRI contrast agent (Fig. 7C). The contrast between the tumor location and the surrounding normal tissue might be improved by MNPT, according to the calculated CNR values of the tumor tissue to the surrounding normal tissue, which are displayed in Fig. 7D.

4. Conclusions

In this study, we successfully constructed MNPT. MNPT had good biocompatibility and anticancer effects when utilized in PDT. MNPT generated O_2 and ·OH through CAT and POD activities. The produced O_2 improved the PDT by reducing tumor hypoxia. Increased photosensitizer retention time could also improve the PDT effect. The overproduction of ROS enhanced the tumor-killing effect and immunotherapy. In addition, MNPT provided dual-modality fluorescence-magnetic resonance imaging, real-time monitoring, and feedback on treatment effects. In conclusion, MNPT represents a potential comprehensive construction strategy for improving cancer treatment.

CRediT author statement

Chen Bai: Conceptualization, Methodology, Reviewing and Editing, Funding acquisition; **Jiajing Liu**: Investigation, Validation, Writing – Original draft; **Luyao Bai:** Investigation, Writing – Original draft; **Dapeng Yao**: Validation, Data curation; **Xiaofeng Li**:

Validation, Data curation; **Haoran Zhang**: Investigation; **Dong Guo**: Supervision, Writing – Reviewing and Editing.

Declaration of competing interest

The authors declare that there are no conflicts of interest.

Acknowledgments

This work was supported by the National Natural Science Foundation of China (Gtant No.: 32201169) and the Natural Science Foundation of Jiangsu Province (Grant No.: BK20220662). We thank Dr. Fuxing Dong from the Public Experimental Research Center of Xuzhou Medical University for the help with the confocal microscope (Leica, STELLARIS 5) experiment.

Appendix A. Supplementary data

Supplementary data to this article can be found online at https://doi.org/10.1016/j.jpha.2023.12.018.

References

[1] N.M. Idris, M.K. Gnanasammandhan, J. Zhang, et al., *In vivo* photodynamic therapy using upconversion nanoparticles as remote-controlled nanotransducers, Nat. Med. 18 (2012) 1580–1585.
[2] T. Zhang, Y. Sun, J. Cao, et al., Intrinsic nucleus-targeted ultra-small metal-organic framework for the type I sonodynamic treatment of orthotopic pancreatic carcinoma, J. Nanobiotechnology 19 (2021), 315.
[3] B. Yang, Y. Chen, J. Shi, Nanocatalytic medicine, Adv. Mater. 31 (2019), e1901778.
[4] L. Zhang, C.-X. Li, S.-S. Wan, et al., Nanocatalyst-mediated chemodynamic tumor therapy, Adv. Healthc. Mater. 11 (2022), e2101971.
[5] Y. Han, S. Gao, Y. Zhang, et al., Metal-based nanocatalyst for combined cancer therapeutics, Bioconjug. Chem. 31 (2020) 1247–1258.
[6] L. Zhu, Y. Dai, L. Gao, et al., Tumor microenvironment-modulated nanozymes for NIR-II-triggered hyperthermia-enhanced photo-nanocatalytic therapy via disrupting ROS homeostasis, Int. J. Nanomedicine 16 (2021) 4559–4577.
[7] X. Han, Y. Li, Y. Zhou, et al., Metal-organic frameworks-derived bimetallic nanozyme platform enhances cytotoxic effect of photodynamic therapy in hypoxic cancer cells, Mater. Des. 204 (2021), 109646.
[8] N. Sobhani, A.A. Samadani, Implications of photodynamic cancer therapy: An overview of PDT mechanisms basically and practically, J. Egypt. Natl. Canc. Inst. 33 (2021), 34.
[9] B. Niu, K. Liao, Y. Zhou, et al., Application of glutathione depletion in cancer therapy: Enhanced ROS-based therapy, ferroptosis, and chemotherapy, Biomaterials 277 (2021), 121110.
[10] Q. Liu, X. Ding, X. Xu, et al., Tumor-targeted hyaluronic acid-based oxidative stress nanoamplifier with ROS generation and GSH depletion for antitumor therapy, Int. J. Biol. Macromol. 207 (2022) 771–783.
[11] S. Kwiatkowski, B. Knap, D. Przystupski, et al., Photodynamic therapy-mechanisms, photosensitizers and combinations, Biomed. Pharmacother. 106 (2018) 1098–1107.
[12] Y. Sheng, H. Nesbitt, B. Callan, et al., Oxygen generating nanoparticles for improved photodynamic therapy of hypoxic tumours, J. Control. Release 264 (2017) 333–340.
[13] X. Wang, X. Zhong, Z. Liu, et al., Recent progress of chemodynamic therapy-induced combination cancer therapy, Nano Today 35 (2020), 100946.
[14] T. Hu, Z. Wang, W. Shen, et al., Recent advances in innovative strategies for enhanced cancer photodynamic therapy, Theranostics 11 (2021) 3278–3300.
[15] S. Gao, Y. Jin, K. Ge, et al., Self-supply of O_2 and H_2O_2 by a nanocatalytic medicine to enhance combined chemo/chemodynamic therapy, Adv. Sci. (Weinh.) 6 (2019), 1902137.
[16] L.-H. Fu, Y. Wan, C. Qi, et al., Nanocatalytic theranostics with glutathione depletion and enhanced reactive oxygen species generation for efficient cancer therapy, Adv. Mater. 33 (2021), e2006892.
[17] C.D. Phung, T.H. Tran, L.M. Pham, et al., Current developments in nanotechnology for improved cancer treatment, focusing on tumor hypoxia, J. Control. Release 324 (2020) 413–429.
[18] W. Fan, B. Yung, P. Huang, et al., Nanotechnology for multimodal synergistic cancer therapy, Chem. Rev. 117 (2017) 13566–13638.
[19] Z. Fu, D. Ni, S. Cai, et al., Versatile BP/Pd-FPEI-CpG nanocomposite for "three-in-one" multimodal tumor therapy, Nano Today 46 (2022), 101590.
[20] Y. Liu, S. Zhai, X. Jiang, et al., Intracellular mutual promotion of redox homeostasis regulation and iron metabolism disruption for enduring chemodynamic therapy, Adv. Funct. Mater. 31 (2021), 2010390.
[21] D. Liu, H. He, F. Kong, et al., A versatile metal-organic nanoplatform in combination with CXCR4 antagonist and PD-L1 inhibitor for multimodal synergistic cancer therapy and MRI-guided tumor imaging, Nano Today 47 (2022), 101689.
[22] R. Antwi-Baah, Y. Wang, X. Chen, et al., Hybrid morphologies of paramagnetic manganese-based nanoparticles as theranostics, Chem. Eng. J. 466 (2023), 142970.
[23] W. Wu, Y. Pu, X. Lu, et al., Transitional metal-based noncatalytic medicine for tumor therapy, Adv. Healthc. Mater. 10 (2021), e2001819.
[24] G. Gunaydin, M.E. Gedik, S. Ayan, Photodynamic therapy-current limitations and novel approaches, Front. Chem. 9 (2021), 691697.
[25] L. Larue, B. Myrzakhmetov, A. Ben-Mihoub, et al., Fighting hypoxia to improve PDT, Pharmaceuticals 12 (2019) 163.
[26] A.M. Negrescu, M.S. Killian, S.N.V. Raghu, et al., Metal oxide nanoparticles: Review of synthesis, characterization and biological effects, J. Funct. Biomater. 13 (2022), 274.
[27] J. Bonet-Aleta, J. Calzada-Funes, J.L. Hueso, Manganese oxide nano-platforms in cancer therapy: Recent advances on the development of synergistic strategies targeting the tumor microenvironment, Appl. Mater. Today 29 (2022), 101628.
[28] S. Dong, Y. Dong, B. Liu, et al., Guiding transition metal-doped hollow cerium tandem nanozymes with elaborately regulated multi-enzymatic activities for intensive chemodynamic therapy, Adv. Mater. 34 (2022), e2107054.
[29] Y. Wang, M. Wang, M.N. Djekidel, et al., eccDNAs are apoptotic products with high innate immunostimulatory activity, Nature 599 (2021) 308–314.
[30] C. Bai, P. Hu, N. Liu, et al., Synthesis of ultrasmall Fe_3O_4 nanoparticles as T_1-T_2 dual-modal magnetic resonance imaging contrast agents in rabbit hepatic tumors, ACS Appl. Nano Mater. 3 (2020) 3585–3595.
[31] A. Farzin, S.A. Etesami, J. Quint, et al., Magnetic nanoparticles in cancer therapy and diagnosis, Adv. Healthc. Mater. 9 (2020), e1901058.
[32] L. Dai, X. Li, X. Zheng, et al., TGF-β blockade-improved chemo-immunotherapy with pH/ROS cascade-responsive micelle via tumor microenvironment remodeling, Biomaterials 276 (2021), 121010.
[33] J. Ma, W. Li, J. Li, et al., A small molecular pH-dependent fluorescent probe for cancer cell imaging in living cell, Talanta 182 (2018) 464–469.
[34] J. Bonet-Aleta, M. Sancho-Albero, J. Calzada-Funes, et al., Glutathione-Triggered catalytic response of Copper-Iron mixed oxide Nanoparticles. Leveraging tumor microenvironment conditions for chemodynamic therapy, J. Colloid Interface Sci. 617 (2022) 704–717.
[35] G. Yang, J. Ji, Z. Liu, Multifunctional MnO_2 nanoparticles for tumor microenvironment modulation and cancer therapy, Wiley Interdiscip. Rev. Nanomed. Nanobiotechnol. 13 (2021), e1720.
[36] L. Meng, J. Feng, J. Gao, et al., Reactive oxygen species- and cell-free DNA-scavenging Mn_3O_4 nanozymes for acute kidney injury therapy, ACS Appl. Mater. Interfaces 14 (2022) 50649–50663.
[37] Q. Liu, A. Zhang, R. Wang, et al., A review on metal- and metal oxide-based nanozymes: Properties, mechanisms, and applications, Nanomicro Lett. 13 (2021), 154.
[38] L. Gao, J. Zhuang, L. Nie, et al., Intrinsic peroxidase-like activity of ferromagnetic nanoparticles, Nat. Nanotechnol. 2 (2007) 577–583.
[39] Z. Chu, J. Yang, W. Zheng, et al., Recent advances on modulation of H_2O_2 in tumor microenvironment for enhanced cancer therapeutic efficacy, Coord. Chem. Rev. 481 (2023), 215049.
[40] P. Urbán, N.J. Liptrott, S. Bremer, Overview of the blood compatibility of nanomedicines: A trend analysis of *in vitro* and *in vivo* studies, Wiley Interdiscip. Rev. Nanomed. Nanobiotechnol. 11 (2019), e1546.
[41] I. Taniuchi, CD4 helper and CD8 cytotoxic T cell differentiation, Annu. Rev. Immunol. 36 (2018) 579–601.
[42] A. Hak, M.S. Ali, S.A. Sankaranarayanan, et al., Chlorin e6: A promising photosensitizer in photo-based cancer nanomedicine, ACS Appl. Bio Mater. 6 (2023) 349–364.